Geochimica et Cosmochimica Acta 433 (2026) 190–199

Contents lists available at ScienceDirect

Geochimica et Cosmochimica Acta

journal homepage: www.elsevier.com/locate/gca

Impact-induced formation of low-Ca pyroxene in a partially melted troctolitic clast from the Chang'e-5 lunar regolith

Yang Bai [a], Zhuang Guo [a,*], Yuqi Qian [b], Shichuan Sun [c], Jingru Ma [a], Kangjun Huang [a], Li-Hui Chen [a], Yunpeng Dong [a], Simon A.T. Redfern [c], Charles K. Shearer [d], Guochun Zhao [a,b]

[a] State Key Laboratory of Continental Evolution and Early Life, NWU-HKU Joint Center of Earth and Planetary Sciences, Department of Geology, Northwest University, Xi'an 710069, China
[b] NWU-HKU Joint Center of Earth and Planetary Sciences, Department of Earth and Planetary Sciences, The University of Hong Kong, Hong Kong, China
[c] Asian School of the Environment, Nanyang Technological University, 50 Nanyang Avenue, Singapore 639798, Singapore
[d] Institute of Meteoritics, Department of Earth and Planetary Sciences, University of New Mexico, Albuquerque, NM 87131, USA

ARTICLE INFO

Associate Editor: Nicholas J. Dygert

Keywords:
Mg-suite rock
Low-Ca pyroxene
Lunar deep materials
Chang'e-5 lunar soil

ABSTRACT

The composition of the lunar deep interior remains debated, as remote sensing observations indicate that impact-excavated materials from within and around large basins contain both olivine and low-Ca pyroxene (LCP). Here we show a partially melted exotic troctolitic clast from Chang'e-5 lunar soils that records impact-induced mineral transformations. The exotic clast consists of forsteritic olivine grains with magnesium-rich rims and pyroxene crystals embedded in a feldspathic glassy matrix. Pyroxene crystals occur as elongated aggregates, with dendritic crystallites growing along the grain edges. The elongated pyroxene crystals show distinct zoning, with Fe-enriched, low-Ca cores and Al-enriched, high-Ca rims, while the dendritic crystallites are compositionally identical to the rims. Elemental mass-balance considerations suggest that impact-induced melting and recrystallization of olivine and anorthite generated the observed LCP–Al-rich high-Ca pyroxene (HCP) assemblage, with Si released during anorthite transformation compensating for the substantial Si consumption during LCP formation. These observations indicate that the LCP formed through impact-induced partial melting of an olivine-rich troctolite under rapid cooling conditions, rather than being a primary phase excavated from the lunar deep interior. Our findings demonstrate that LCP signatures observed around large impact basins, e.g., Imbrium and South Pole-Aitken basins, may originate from impact-modified olivine-rich lithologies, rather than being directly excavated from the deep interior. These results raise the possibility that such transformations may be a widespread process associated with large-scale impacts on the Moon and have important implications for the interpretation of remote sensing data and constraints on the composition of the lunar interior.

1. Introduction

The precise characterization of the lunar deep-seated materials is crucial for constraining both the lunar internal structure and early magma ocean processes (Dickey et al., 1994; Khan et al., 2013; Wieczorek et al., 2006). To date, only a few lunar mantle samples have been identified (Sheng et al., 2025), but the exact mineralogical composition of the Moon's deep interior remains a subject of ongoing debate (Klima et al., 2011; Yamamoto et al., 2023). Based on remote sensing observations, olivine-enriched lithologies have been found to concentrate around impact basins with thin crustal thickness, such as the Moscoviense, Crisium, and Imbrium basins (Yamamoto et al., 2022). These observations are consistent with the hypothesis proposed by Wieczorek et al. (2013) that olivine may directly underlie the lunar crust. However, mafic minerals surrounding the South Pole–Aitken (SPA) basin are predominantly low-Ca pyroxene (LCP; Wo < 15) (Sun and Lucey, 2024), suggesting that material excavated from the Moon's deep-seated interior by large impact events is primarily composed of LCP (Lucey et al., 2014; Melosh et al., 2017). Consequently, the question of whether LCP or olivine constitutes the dominant phase in the upper mantle continues to be a matter of active debate.

The exposure of deep-seated lunar materials is typically ascribed to excavation by early, large impact events, including the formation of the SPA basin and the Late Heavy Bombardment (LHB) (Gou et al., 2019;

* Corresponding author.
E-mail address: guozhuang@nwu.edu.cn (Z. Guo).

https://doi.org/10.1016/j.gca.2026.09.038
Received 17 May 2026; Accepted 29 September 2026
Available online 4 October 2026
0016-7037/© 2026 Elsevier Ltd. All rights are reserved, including those for text and data mining, AI training, and similar technologies.

Melosh et al., 2017; Miljković et al., 2015; Potter et al., 2012). Owing to the absence of atmospheric shielding, these excavated lunar materials have undergone prolonged modification and redistribution driven by repeated impact events, reflecting the dynamic evolution of exposed deep-seated materials on the Moon and the alteration of their original mineralogical composition (Miljković et al., 2015; Shearer et al., 2015; Yamamoto et al., 2010). Highly impact-modified magnesian materials (Mg# >72), likely sourced from the mantle, have been identified in lunar soils, displaying granoblastic textures and signs of glassification, consistent with the excavation and high-temperature modification of lunar lithologies by large impacts (Ding et al., 2025; He et al., 2024). Furthermore, LCP is common in impact-modified magnesian granulites, granulitic breccias, and lunar meteorites (Cushing et al., 1999; Lindstrom and Lindstrom, 1986; Roberts et al., 2019), suggesting a link to impact excavation events. Therefore, elucidating the subsequent impact-induced modification of deep-seated lunar minerals is a prerequisite for accurately characterizing the composition of the lunar interior and for interpreting remote-sensing spectra.

The Chang'e-5 mission successfully landed in the northern Oceanus Procellarum region of the Moon, a unit dominated by ~2.0 Ga mare basalts (Wang et al., 2024). The returned lunar soils are primarily composed of fine-grained local basaltic material, with minor contributions from exotic lithologies (Zeng et al., 2023; Zong et al., 2022). Here, we report an exotic troctolitic clast exhibiting characteristic partial melting textures in Chang'e-5 lunar soils. Its petrographic and mineralogical features provide compelling evidence that LCP formed through impact-induced partial melting of a troctolite clast, implying that LCP signatures in lunar impact structures may originate from secondary, impact-modified olivine-rich lithologies.

2. Methods

The studied Chang'e-5 lunar soil sample (~50 mg), designated CE5Z0403YJFM, was allocated by the China National Space Administration. Large lithic grains (>50 μm) were selected, embedded in epoxy resin for stabilization, and subsequently polished and carbon-coated for scanning electron microscopy (SEM) observations.

High-resolution back-scattered electron (BSE) imaging, energy-dispersive X-ray spectroscopy (EDS) analyses, and focused ion beam (FIB) section preparation of the lunar soil sample were performed on a Thermo Scientific Helios G4 UX DualBeam FIB-SEM at the State Key Laboratory of Continental Evolution and Early Life, Northwest University. Chemical analyses of FIB sections, including TEM X-ray elemental mapping and EDS spectral acquisition, were performed using the EDS detector on a Talos F200X scanning transmission electron microscope (STEM). TEM-EDS data were precisely quantified via an interactive method in Bruker Esprit software. High-resolution TEM (HRTEM) images and selected area electron diffraction (SAED) patterns were acquired to determine the crystal structures of minerals within the FIB sections.

Quantitative analyses of the major-element compositions of phases in the studied clast were conducted using a JEOL JXA-iHp200F field-emission electron microprobe (EPMA) at the State Key Laboratory of Continental Evolution and Early Life, Northwest University, China. Analyses were performed with an accelerating voltage of 15 kV and a beam current of 10 nA. The mineral phases of large olivine grains and melted glassy materials were analyzed using a 5–10 μm focused beam, whereas micron-sized pyroxene grains were examined with a 2 μm beam. Natural and synthetic minerals served as standards, with typical detection limits for most elements below 0.02 wt%. ZAF corrections for silicate and oxide phases utilized albite (Na), olivine (Si, Mg), diopside (Ca), almandine (Fe), pyrope (Al), orthoclase (K), rutile (Ti), rhodonite (Mn), and Cr_2O_3 (Cr). Modal mineralogy (vol% by area) was estimated from EDS X-ray elemental maps, and the bulk composition of the studied clast were subsequently derived from the modal mineralogy and EPMA data.

Raman spectra of minerals were acquired using a WITec alpha 300 R laser micro-Raman spectrometer equipped with a Zeiss EC Epiplan objective at the Institute of Geology and Geophysics, Chinese Academy of Sciences. A 532 nm Ar-ion laser with a power of 10 mW was focused onto a ~1 μm spot on the sample under 50 × objective magnification, with an acquisition time of 20 s. All spectra were calibrated against the single-crystal silicon standard peak at 521 cm^{-1}.

3. Results

3.1. Mineral chemistry of the Chang'e-5 exotic clast

The studied exotic clast, approximately 50 × 60 μm in size, is a partially melted lithic clast from the prepared Chang'e-5 polished mount. It is composed primarily of pyroxene (~32 vol%) and olivine (~29 vol%) grains embedded within a feldspathic glassy matrix (~39 vol%), exhibiting a vitrophyric texture (Fig. 1a).

The olivine grains within the glassy matrix exhibit subhedral morphologies with pronounced melting-induced resorption along their edges (Fig. 1a). SEM-EDS mapping and line profile analyses reveal that the olivine grains exhibit reverse zoning, characterized by a progressive increase in Mg and a concomitant decrease in Fe from core to rim (Fig. 1b–f and Line 1 in Fig. 1h). Quantitative EPMA analyses indicate that the olivine grains are highly forsteritic. The FeO content decreases from 9.33 wt% at the core to 6.5 wt% at the rim, whereas MgO content correspondingly increases from 49.5 wt% to 51.9 wt% (Table 1). The calculated Fo values increase from 90.4 at the core to 93.4 at the rim, with an average Fo of 92.1 in the core (Fig. 2c, Table 1), further confirming the pronounced chemical zonation. The Raman spectra of the analyzed olivine exhibit prominent peaks at 822 cm^{-1} and 854 cm^{-1}, along with additional peaks at 917 cm^{-1} and 960 cm^{-1}, consistent with standard forsterite spectra from the RRUFF database (Fig. S1).

SEM observations show that pyroxene crystals within the glassy matrix occur as elongated micron-sized aggregates (6.65–20.6 μm in length and 1.36–2 μm in width) and exhibit sharp compositional zonation with rim widths of <1 μm (Fig. 1a, g). Numerous nano-sized dendritic crystallites extend perpendicularly from the sides of the elongated crystals along their long axes and display BSE contrast identical to that of the pyroxene rims (Fig. S2). EDS elemental maps and line profiles reveal an abrupt compositional transition between cores and rims. The cores are characterized by low Ca contents (<5 at%; Fig. 1h) and relatively higher Fe abundances, whereas the rims and dendritic crystallites are enriched in Al and Ca (Fig. 1g; Line 2 in Fig. 1h). Because the rims are narrower than the EPMA probe diameter, their compositions cannot be quantified exactly. EPMA analyses show that the pyroxenes have low CaO contents (2.53–5.16 wt%) and span a compositional range of $En_{52–64.9}Fs_{28.8–36.7}Wo_{5.31–11.3}$, with high Mg# values of 58.6–69.2 (average = 63.7; Table 1, Fig. 2d). Atomic Fe/Mn ratios of the pyroxenes fall within the compositional field of Chang'e-5 basalts, confirming the lunar origin of this exotic clast (Fig. 2a). Raman spectra from these pyroxene grains display strong peaks at 323 cm^{-1}, 669 cm^{-1} and 997 cm^{-1}, consistent with reference pigeonite spectra from the RRUFF database (Fig. S1). Additional peaks at 822 cm^{-1} and 854 cm^{-1} are attributable to spatially associated olivine grains (Fig. S1).

The glassy matrix of the exotic clast is highly heterogeneous, hosting numerous spherical and needle-like crystallites (Fig. 1a). No other residual mineral phases were observed aside from scattered remnants of fine-grained olivine (Fig. 1d). It is enriched in CaO (~10.3 wt%) and Al_2O_3 (~17.7 wt%), with a low MgO/Al_2O_3 ratio of ~0.66 (Table 1). This composition substantially deviates from that of Apollo pyroclastic glasses and local basaltic impact glasses from the Chang'e-5 landing site, instead falling within the compositional field of lunar highland glasses (Fig. 2b). Based on modal mineralogy and the average EPMA chemistry of each phase, the bulk composition of the exotic clast was calculated as 47.8 wt% SiO_2, 5.2 wt% CaO, 25.6 wt% MgO, 12.1 wt% FeO, 7.5 wt% Al_2O_3, and 0.87 wt% TiO_2 (Table S1).

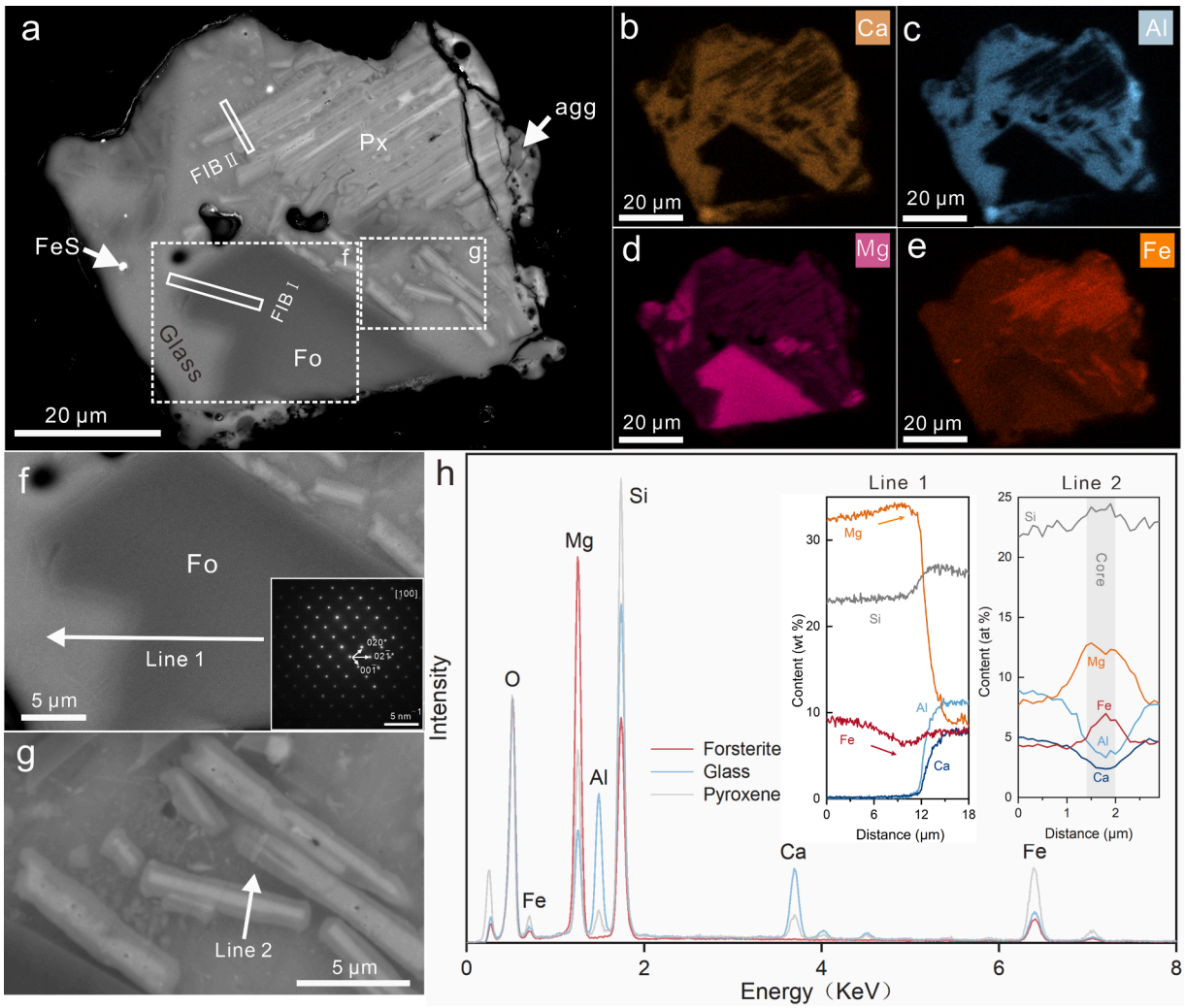

Fig. 1. BSE images, X-ray maps, and EDS line results of the exotic clast. (a) The exotic clast is composed of partially melted olivine grains, elongated pyroxene crystals, and a glassy matrix, and shows the positions where two FIB foils (FIB-I and FIB-II) were extracted from olivine and pyroxene, respectively. (b–e) X-ray maps of the exotic clast. (f) Magnified image and SEM-EDS line scan profile of olivine. (g) Magnified image and SEM-EDS line scan profile of pyroxene. The selected area electron diffraction (SAED) pattern of olivine is shown in the bottom right of the figure. (h) Result of SEM-EDS line profiles. Note that olivine grains show a slight compositional zoning with Mg-rich rims and slightly Fe-rich cores, while pyroxene crystals show a thin contrasting zonation feature with a typical low-calcium characteristic. Px: pyroxene; Fo: forsteritic olivine.

3.2. *Microscopic characteristics of the mineralogy in the exotic clast*

Two focused ion beam (FIB) foils, designated FIB-I and FIB-II, were extracted from the zoned olivine and elongated pyroxene within the exotic clast, respectively, for detailed mineralogical characterization using transmission electron microscopy (TEM) (Fig. 1a). Selected area electron diffraction (SAED) patterns of olivine along the [100] zone axis reveal (020) lattice fringes with a spacing of 5.15 Å, and the angle between the (020) and (02$\bar{1}$) is measured at 40.5°, consistent with the crystal structure of forsterite (Fig. 1f; Fig. S3).

Bright-field TEM imaging of the FIB-II foil reveals that the elongated pyroxene exhibits multiple crystallographic orientations, with numerous crystallites nucleating and growing along the grain edges, corresponding to the dendritic crystallites observed in SEM images (Fig. 3a, 3d; Fig. S2). Distinct compositional zoning in pyroxene is clearly resolved in TEM images, with rim widths measuring less than 200 nm (Fig. 3d). TEM-EDS X-ray elemental mapping further highlights compositional contrasts between the cores and rims of the elongated pyroxene (Fig. 3i–l). The cores are enriched in Fe, whereas the rims show lower Fe concentrations and relatively higher Al and Ca contents (Fig. 3j–l). Quantitative TEM-EDS analysis indicates that the pyroxene cores contain an average Ca content of 0.36 at%, while the rims are enriched to 3.84 at%, corresponding to Wo values of 3.7 and 21.5, respectively (Table S2). SAED patterns acquired from the pyroxene core along multiple zone axes confirm its crystal structure as low-Ca clinopyroxene. Along the [110] zone axis, ($\bar{1}$10) lattice fringes with a d-spacing of 6.42 Å and an angle of 60.5° between the ($\bar{1}$10) and ($\bar{1}$11) planes (Fig. 3b). A complementary SAED pattern along the [020] zone axis revealed (100) lattice fringes with a periodicity of 9.2 Å, and the angle between the (100) and (20$\bar{2}$) planes was measured to be 76.8° (Fig. 3c). All measured structural parameters are fully consistent with the crystal structure of pigeonite, confirming that the pyroxene core is

Table 1
Average EPMA compositions (wt%) of minerals and olivine EPMA line scan results from the exotic clast.

	Olivine		Pyroxene		Glass matrix		Olivine line scan			
wt%	n = 2	1-σ	n = 3	1-σ	n = 3	1-σ	Ol line-1(core)	Ol line-2	Ol line-3	Ol line-4
SiO_2	41.3	0.08	52.0	1.56	49.3	1.03	41.6	41.9	41.9	42.0
TiO_2	0.03	0.02	0.84	0.10	1.51	0.12	0.02	0.01	0.01	0.02
Al_2O_3	0.07	0.03	1.80	1.75	17.7	0.31	0.04	0.04	0.05	0.13
Cr_2O_3	—	—	—	—	—	—	0.05	0.06	0.07	0.16
FeO	7.68	0.70	20.1	1.94	8.90	0.95	9.33	9.05	7.72	6.50
MnO	0.08	0.01	0.37	0.03	0.15	0.04	0.10	0.09	0.08	0.07
MgO	50.5	0.56	19.8	1.46	11.8	0.92	49.5	50.5	51.3	51.9
CaO	0.19	0.10	3.55	0.99	10.3	0.30	0.09	0.08	0.16	0.28
NiO	0.03	0.02	b.d.	b.d.	0.03	0.02				
Na_2O	—	—	0.07	0.02	0.27	0.05				
K_2O	—	—	0.03	0.00	0.21	0.01				
F	—	—	0.04	0.00	b.d.	b.d.				
Cl	—	—	0.02	0.00	0.02	0.01				
Total	99.9		98.6		100.1		100.7	101.7	101.3	101.0
Formula (O = 24)										
Si	6.01		7.85		7.02		6.04	6.03	6.02	6.01
Ti	—		0.10		0.16		—	—	—	—
Al	0.01		0.32		2.96		0.01	0.01	0.01	0.02
Cr	—		—		—		0.01	0.01	0.01	0.02
Fe	0.94		2.54		1.06		1.13	1.09	0.93	0.78
Mn	0.01		0.05		0.02		0.01	0.01	0.01	0.01
Mg	11.0		4.45		2.50		10.7	10.8	11.0	11.1
Ca	0.03		0.58		1.58		0.01	0.01	0.02	0.04
Ni	0.01		b.d.		b.d.					
Na	—		0.02		0.08					
K	—		b.d.		0.04					
Fe/Mn	104		54.1		58.7		90.6	95.8	97.6	92.3
Mg# (Fo)	92.1		63.7		70.2		90.4	90.9	92.2	93.4
Wo			7.63							
En			58.8							
Fs			33.6							

Note. b.d.: below detection limit.

LCP.

TEM-EDS X-ray elemental mapping reveals that the pyroxene rims and the spherical and needle-like nanoscale crystallites within the glassy matrix of the exotic clast share identical compositions (Fig. 3h–l). High-resolution TEM images of both the pyroxene rims and the nanoscale crystallites indicate a similar clinopyroxene crystal structure (Fig. 3f, g). Integrating the chemical (Table S2) and structural data, the low-Ca cores are confirmed to be pigeonite, whereas the high-Ca rims and crystallites are dominated by augite.

4. Discussion

4.1. Petrography of the Chang'e-5 exotic clast

The studied exotic clast exhibits petrographic and compositional characteristics distinct from the local Chang'e-5 mare basalts (Fig. 2b–d). Pyroxenes within the exotic clast have an atomic Fe/Mn ratio of ~54.1, while the glassy matrix is enriched in Ca and depleted in Na and K (Table S1), consistent with lunar mineralogical chemistry and indicating a lunar origin (Fig. 2a). Notably, the olivine displays exceptionally high forsterite content (an average Fo value of 92.1), markedly more magnesium-rich than olivine in Chang'e-5 basalts ($Fo_{\sim 37.2}$) (Li et al., 2022). The pyroxene in the exotic clast exhibits a markedly higher Mg# (~63.7) than Chang'e-5 mare basalt pyroxenes (~32.1), reflecting the overall magnesium-rich nature of the exotic clast's bulk composition (Li et al., 2022; Tian et al., 2021). Moreover, the glassy matrix exhibits low MgO/Al_2O_3 ratios, inconsistent with local basaltic glasses but consistent with a post-impact (see Section 4.2), plagioclase-rich melt enriched in Ca and Al. Together, these observations indicate that the studied exotic clast represents an exotic, ejected lithology originating from outside the basaltic terrain of the Chang'e-5 landing site, and its petrology resembles that of lunar Mg-suite rocks. However, the embayed resorption features of olivine and the high proportion of glass within the exotic clast indicate extensive impact-induced melting (see Section 4.2), which has obscured the original petrographic characteristics.

Troctolites and norites represent the two most common lithologies of Mg-suite rocks identified in lunar samples. In the exotic clast, the olivine grains display reverse zoning, characterized by Mg-rich rims and relatively Fe-rich cores, reflecting partial melting during which the low-melting-point fayalite component preferentially partitioned into the melt at the grain margins. Consequently, the olivine cores likely preserve the initial chemical composition of the original lithology. The residual olivine grain exhibits coarse-grained, subhedral morphologies and accounts for ~29 vol% of the exotic clast, indicating that the original lithology was olivine-dominated. The glassy matrix (~39 vol%) is enriched in Al and Ca, with an approximate atomic Ca/Al ratio of 1:2 (Fig. 1b, c, h; Table 1), suggesting that it is likely derived from the complete melting of primary anorthite ($CaAl_2Si_2O_8$). The pristine olivine in the exotic clast exhibits an exceptionally high Mg# (~92.1), which lies at the upper end of typical troctolite values (Mg# 83–92) (Hess, 1994) and is significantly higher than those of norites (Mg# 70–86) (Heiken et al., 1991; Warren, 1993). Based on the atomic Ca/(Ca + Na + K) ratio of the glass, the An content of the original plagioclase is estimated to exceed 90. Accordingly, the exotic clast is dominated by forsteritic olivine and plagioclase and plots within the field of magnesium troctolite on a diagram of plagioclase An# versus olivine Mg# (Gross et al., 2014; Shervais and McGee, 1999b) (Fig. S4). Olivines from Mg-suite lithologies typically have lower Cr and Ni contents, and most olivine Ni contents are less than 300 ppm (Shearer et al., 2015). The average Ni content of olivine from the exotic clast determined by EPMA is 280 ppm (Table S1). Additionally, the exotic clast falls within the field

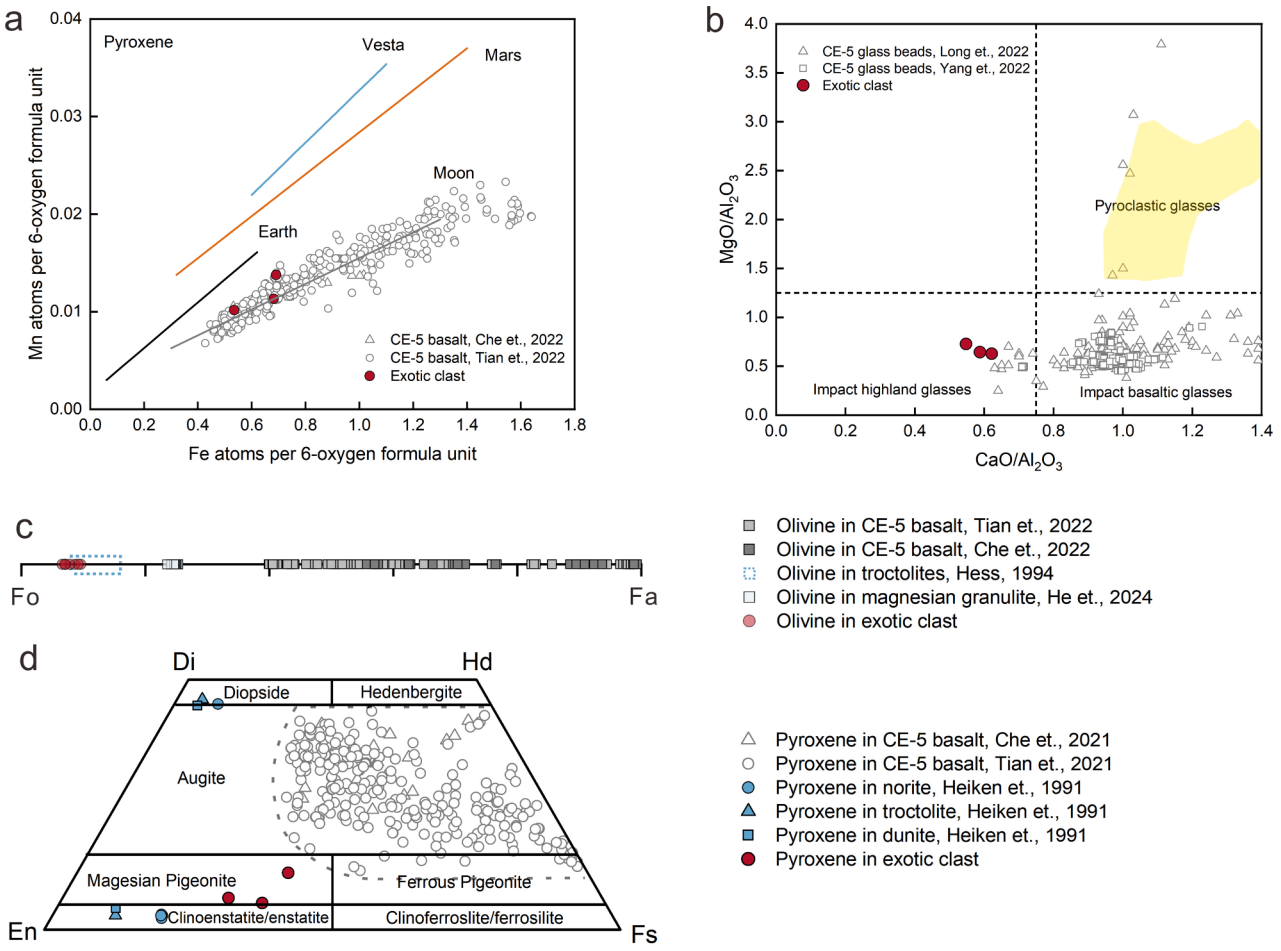

Fig. 2. Comparison of mineral chemistry in the exotic clast in relation to Mg-suite and basalt rocks. (a) Mn vs Fe atoms per 6-oxygen formula unit in pyroxene of the exotic clast in relation to Chang'e-5 mare basalt (Che et al., 2021; Tian et al., 2021). Planetary trend lines are from Papike et al. (2009). (b) CaO/Al_2O_3 versus MgO/Al_2O_3 diagram of the exotic clast. The Chang'e-5 glass data are from Long et al., (2022) and Yang et al., (2022). The yellow area denotes the picritic volcanic glass after Delano (1986). (c) Olivine mineral composition within the exotic clast. Troctolite's data are from Hess (1994). Magnesian granulite data of Chang'e-5 samples are from He et al. (2024). (d) Quadrilateral diagram of pyroxene in the exotic clast. Data for norite, troctolite, and dunite are from Heiken et al. (1991).

of Mg-suite rocks on a plot of Cr in parts per million vs. Mg# in olivine (Fig. S5). Although LCP is also confirmed as a dominant component within the exotic clast, its monoclinic crystal structure, rather than an orthorhombic structure (i.e., hypersthene), is inconsistent with the typical mineralogy of norite (Crites et al., 2015; Papike et al., 1994; Shervais and McGee, 1999a; Shervais et al., 1983). These observations indicate that magnesium troctolite represents the most likely precursor lithology of the studied Chang'e-5 exotic clast rather than a noritic precursor.

The bulk composition of the Chang'e-5 exotic clast is characterized by high MgO and FeO contents and relatively low Al_2O_3 and CaO concentrations (~25.6 wt% MgO, ~12.1 wt% FeO, ~7.5 wt% Al_2O_3, ~5.2 wt% CaO). These geochemical characteristics closely resemble those of samples returned from the Apollo 14 site of the Fra Mauro highlands (Fig. S6) (Jolliff et al., 2006; Shervais and McGee, 1999b). Apollo 14 samples have been shown to contain a significant proportion of Imbrium basin ejecta, collectively referred to as the Fra Mauro Formation (Dence and Plant, 1972; Jolliff et al., 2006; Morrison and Oberbeck, 1975; Nemchin et al., 2009). Based on studies of relatively pristine highland samples from Apollo 14, Shervais and McGee (1999b) proposed that lunar troctolites can be divided into two distinct groups: Group I, characterized by plagioclase of $An_{94–95}$, olivine of $Fo_{87–89}$, and pyroxene with Mg# values of 88–90; and Group II, containing olivine with $Fo_{67–85}$ and pyroxene with Mg# values of 70–88. The composition of the exotic clast falls within the compositional range of Group I troctolites.

Lunar Mg-suites are generally considered to have formed through the intrusion of deep-seated, mafic parent magmas into the anorthositic lunar crust (Shearer et al., 2015). By assuming an equilibrium Fe-Mg exchange distribution coefficient (K_D) of 0.30–0.33 for lunar systems (Longhi, 1978), the reverse-zoned olivine cores (Fo = 92.1, Table S1) in the studied clast—which best preserve the primary pre-impact magmatic signature—yield a calculated parental melt Mg# ranging from 77.8 to 79.4. This extraordinarily high Mg# indicates a highly primitive magma, surpassing the Mg# (~60–68) of typical lunar picritic volcanic glasses, which are generally considered the most primitive partial melts of the lunar interior (Delano, 1986; Shearer and Papike, 1993). This compositional affinity is highly consistent with the calculated primitive mantle-derived parental magmas of the Mg-suite cumulates (e.g., troctolites and dunites) returned from the Apollo 14 site (Shearer et al., 2015; Shervais and McGee, 1999b; Warren, 1993). Besides, the combination of highly magnesian olivine (Fo ≈ 92) and depleted Ni contents (~280 ppm) indicates that the parental magma was likely derived from a shallow-level hybridized mantle source (Shearer and Papike, 2005; Jolliff et al., 2006). Such a primitive magma composition suggests that the parent magma may have formed in the lunar mantle, rapidly ascended through the mantle, and intruded into

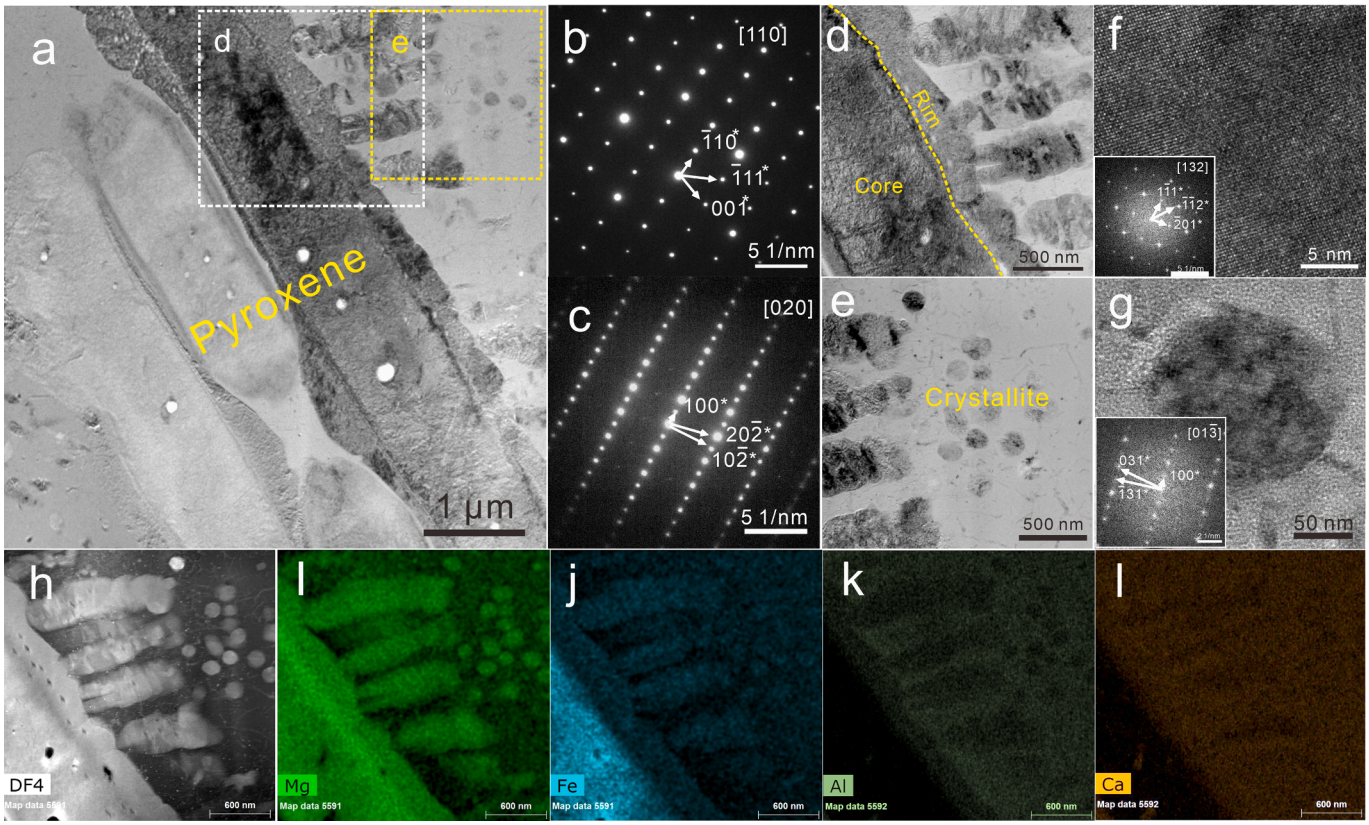

Fig. 3. Transmission electron microscopy (TEM) analyses of elongated pyroxene crystals in the exotic clast. (a) TEM bright-field images of FIB-II. (b–c) SAED patterns of the core. d Enlarged detail view of (a), showing distinct compositional zoning between the core and the rim in pyroxene. e Enlarged detail view of (a), showing the dendritic crystals and crystallites of pyroxene. (f) High-resolution TEM image of the rim. The fast Fourier transform (FFT) pattern is shown in the insert at the bottom left of the figure. (g) High-resolution TEM image of the dendritic crystals. The FFT pattern is shown in the bottom left of the figure. (h–l) X-ray elemental maps of Mg, Fe, Al, and Ca in FIB-II, showing a distinct compositional difference between the core and the rim.

the lower crust (Hess, 1994; Shearer et al., 2015; Snyder et al., 1995).

4.2. An Impact-related origin for low-Ca pyroxene

This exotic clast represents an impact-modified troctolitic fragment, as evidenced by a combination of petrographic, mineralogical, and geochemical features: (1) resorption textures and reverse compositional zoning of olivine and abundant glassy matrix (Fig. 1) indicating partial melting, (2) dendritic pyroxene morphologies and chemical zoning consistent with rapid quenching from a supercooled impact melt (Fig. 3, see below), and (3) a bulk composition distinct from pristine cumulate troctolites (Fig. S6) and the glass composition falling within the impact highland glass field (Fig. 2b). These observations collectively point to impact-induced partial melting rather than a magmatic or volcanic origin. To date, only a few studies have described troctolites that have undergone impact-related transformation, including the Chang'e-5 troctolitic granulite (He et al., 2024), the moderately shock-metamorphosed meteorite NWA 11515 (Li et al., 2025), and high-Mg impact glass beads in Chang'e-5 samples interpreted to originate from the lunar upper mantle (Ding et al., 2025). Here, we report distinctive evidence for impact-induced partial melting of a troctolitic lithology. The exotic clast preserves both pre-impact primary materials and products formed during the impact event. According to the progressive stages of shock metamorphism in the classification system for mafic rocks (Stöffler et al., 2018), the melted plagioclase glass and contact-melted forsterite within the exotic clast indicate a shock stage of S6, with a post-shock temperature above 1100 °C. Such shock conditions are unique to impact events and cannot be achieved by lunar magmatic or volcanic processes.

LCP grains within the exotic clast exhibit an elongated, prismatic habit and are surrounded by numerous dendritic crystallites. This morphology contrasts with the porphyritic or subhedral textures commonly observed in intrusive rocks and instead reflects preferential crystal growth along crystallographic directions with the strongest atomic bonding and fastest growth rates under rapid cooling conditions (Bouquain et al., 2014; Donaldson et al., 1977; Kirkpatrick, 1975). Chemically, pyroxenes in lunar troctolites and norites typically exhibit high Mg# values, generally ranging from ~80 to 99.2 (Gross et al., 2020; Heiken et al., 1991; Wang et al., 2025), and from ~70 to 90 in troctolites from the Apollo 14 site (Shervais and McGee, 1999b). In contrast, the exotic clast investigated here contains pyroxenes with significantly lower Mg# values, ranging from 58.6 to 69.2 (Fig. 2d). Furthermore, the pyroxenes display distinct core-to-rim zoning, with Fe-rich and Ca-poor cores grading to more Ca-rich rims. This pattern is consistent with normal crystallization from an evolving melt through a pigeonite-to-augite crystallization sequence (Fowler et al., 1994; Ginibre et al., 2007; Papike, 1996; Streck, 2008). Such zoning contrasts with the reverse zoning observed in olivine formed during impact-induced partial melting within the exotic clast. In addition, if these pyroxenes were primary and excavated from depth, they would be expected to exhibit exsolution features such as those noted by McCallum and O'Brien (1996) and Marks et al. (2019), but this phenomenon was not observed in our sample. Collectively, these observations indicate that the nano-scale LCP grains within the exotic clast most likely represent secondary phases crystallized from a rapidly cooled, impact-generated troctolitic melt, rather than primary minerals representing the original lithology.

From a chemical mass-balance perspective, olivine should provide the primary mafic elements for LCP formation. However, the transformation of olivine to LCP requires substantial Si, potentially depleting Si in the melt or necessitating an additional Si source. In addition to LCP,

the matrix of the exotic clast contains abundant Al-rich, high-Ca pyroxene (HCP) crystallites and dendrites (Fig. 3 and Table S2), indicating that anorthite also participated in the reaction. Anorthite ($CaAl_2Si_2O_8$) could have supplied Ca and Al for the formation of Al-rich HCP ($CaAl_2SiO_6$, represented here as an idealized Ca–Al-rich pyroxene component). The HCP contains abundant Al (up to 5.69 at%; Table S2), indicating substantial Al substitution for Si in its structure. These chemical characteristics suggest that substantial Si was released during the anorthite-to-HCP transformation. Consequently, the Si budget could be maintained during the melting–recrystallization process, explaining the absence of exceptionally low Si contents in the matrix, consistent with the observed chemical characteristics. Based on the observed mineral phase transformations, the overall reaction can be simplified using idealized endmember compositions to illustrate the elemental mass balance: $CaAl_2Si_2O_8 + (Mg, Fe)_2SiO_4 = 2(Mg, Fe)SiO_3 + CaAl_2SiO_6$. This reaction accounts for both the relatively high Si content of the glassy matrix and the substantial Si consumption associated with LCP formation.

The average Mg# of the glassy matrix is 70.2, whereas that of the pyroxene recrystallized from the melt is 63.7, indicating that the melt was relatively Fe-rich than the remnant forsteritic olivine ($Fo_{92.1}$) (Table 1). In addition, the recrystallized pyroxene exhibits a low Mg# in the core (~51.93) but higher Mg# values at the rims and in the crystallites (~74.5 and 71.9, respectively; Table S2), opposite to the typical compositional evolution of a crystallizing melt. These features indicate that the initial melt was Fe-rich and progressively evolved toward Mg-rich compositions during pyroxene growth, suggesting the progressive addition of Mg-rich material. The observed reverse zoning in olivine further indicates preferential incorporation of the Fe-rich component into the melt at the olivine grain margins, further supporting the formation of an initially Fe-rich melt that progressively evolved toward Mg-rich compositions. Overall, the melting and recrystallization of olivine and anorthite can account for the observed LCP–HCP assemblage from an elemental mass-balance perspective. Moreover, the progressive evolution of melt composition during melting–recrystallization suggests that the matrix of this rock fragment was characterized by pronounced chemical heterogeneity.

On the Moon, impact-induced melts typically cool extremely rapidly, often within less than a second, under strongly supercooled conditions (Chen et al., 2023; Donaldson et al., 1977; Dowty et al., 1974; Morse, 1982; Yakovlev et al., 2011). Donaldson (1979) demonstrated in a series of isothermal experiments that the columnar and dendritic morphologies of minerals are closely linked to supercooling, and dendritic crystallites are also widely recognized as characteristic products of crystallization from supercooled melts (Donaldson et al., 1977; Kirkpatrick, 1975; Mullins and Sekerka, 1964; Sethian and Straint, 1992). Consistent with these observations, LCP grains in the exotic clast exhibit an elongated, prismatic habit and are bordered by numerous dendritic crystallites, indicating that they crystallized from a supercooled melt. The extreme cooling rates required for dendritic crystallization are orders of magnitude faster than any lunar volcanic regime (Donaldson et al., 1977; Faure et al., 2003).

Experimental work by Corrigan (1982) showed that strong supercooling ($-\Delta T > 46.5$ °C) substantially lowers the nucleation rate of olivine, kinetically suppressing it relative to pyroxene and plagioclase (Corrigan, 1982). Under these conditions, numerous LCP nuclei form and progressively sequester Fe and Mg into the growing crystals, further inhibiting olivine crystallization. From the viewpoint of classical nucleation theory, such extreme cooling rates push the melt into a strongly supercooled state in which crystallization is controlled by diffusion in the melt rather than by interface reactions. The accompanying rise in melt viscosity restricts the long-range mobility of Fe and Mg, so once LCP nucleates, it grows rapidly into elongated, dendritic morphologies characteristic of diffusion-limited growth at large undercoolings. This fast growth locally depletes the melt of mafic components, preventing the system from maintaining the supersaturation required for olivine nucleation and thereby fully suppressing it (Aysal et al., 2023; Kirkpatrick, 1983). Our results indicate that the LCP grains, which bear distinctive compositional signatures, likely crystallized from the impact-generated melt derived from the troctolitic clast under rapid cooling conditions on the Moon, rather than representing the primary mineralogy of the pristine lunar lithology.

4.3. Provenance source of the exotic clast and its implications

Previous studies of Chang'e-5 lunar soils indicate that these samples are predominantly composed of space-weathered and mixed local basaltic materials, with only a minor contribution from exotic lithic components (<10%) (Li et al., 2022; Qian et al., 2021b). Raman spectroscopy indicates that the Chang'e-5 samples contain approximately 5–7% exogenous materials, most likely derived from Mg-suite rocks (Cao et al., 2022). Additionally, highly impact-modified magnesian troctolitic granulite grains have been identified in these soils (He et al., 2024). The studied Chang'e-5 exotic clast exhibits petrographic and compositional characteristics distinct from the local mare basalts, instead reflecting a Mg-suite troctolitic lithology, indicative of an exotic highland source beyond the Chang'e-5 landing site. The exotic clast experienced a high degree of shock metamorphism (S6), consistent with ejection from a relatively large impact crater (>10 km in diameter) outside the Chang'e-5 basaltic mare unit.

The extremely high forsterite ($Fo_{92.1}$) content in olivine and elevated bulk MgO (25.6 wt%) of the exotic clast indicate a lower crustal or upper mantle origin (Hess, 1994; Shervais and McGee, 1999b; Warren, 1993; Wieczorek et al., 2006). Large impact basins, such as the SPA and Imbrium basins, are capable of excavating such deep-seated materials by penetrating the lunar crust (Melosh et al., 2017; Miljković et al., 2015; Wieczorek et al., 2013). The bulk composition and mineral chemistry of the Chang'e-5 exotic clast closely resemble those of samples returned from the Apollo 14 site in the Fra Mauro highlands, which likely originate from Imbrium basin ejecta (Dence and Plant, 1972; Jolliff et al., 2006; Morrison and Oberbeck, 1975; Nemchin et al., 2009). Recently, impact glass beads with unusually high Mg# (79.2–80.1), probably derived from mantle-derived rocks composed of LCP and olivine from the Imbrium basin, have been reported (Ding et al., 2025). In addition, numerical simulations of ejecta transport and impact gardening predict that the regolith at the Chang'e-5 landing site should contain a fraction of distal melt and lithic debris excavated from the Imbrium basin, which is expected in both the surface (0–10 cm) and sub-surface (0–2 m) samples collected by the Chang'e-5 mission (Liu et al., 2021). Therefore, the exotic clast most likely originated from the Imbrium basin ejecta.

Based on spectral data, most of the LCP-rich and olivine signals are widespread along the margins of the Imbrium basin, indicating that this region is enriched in both olivine and LCP (Sun and Lucey, 2024; Yamamoto et al., 2023; Yamamoto et al., 2010). Our data are also consistent with these results (Fig. 4a). Moreover, in the Mons Heng area (a kipuka surrounded by mare basalts), which is the 4th basin ring of the Imbrium basin (Qian et al., 2021a) within the Chang'e-5 landing site area, LCP abundances have been identified (Fig. 4b). Accordingly, we infer that the exotic clast was initially excavated and uplifted by the Imbrium impact, collapsed to form Mons Heng, and was subsequently re-ejected by a later impact into the Chang'e-5 landing area, where it eventually collected (Fig. 4c). However, it is clear that excavated deep-seated lunar materials have undergone prolonged modification and redistribution due to repeated impact events, and their original mineralogy may have been altered. Our results support the view that the LCP observed in these regions can crystallize from an olivine-dominated melt during relatively large-scale impact events. Therefore, the LCP detected around the Imbrium basin (e.g., the elevated LCP of Mons Heng) may not directly represent primary materials excavated from the lunar interior but rather post-impact recrystallized phases.

As previously noted, debate persists over whether the lunar mantle is dominated by olivine or LCP. Our results suggest that a certain portion of

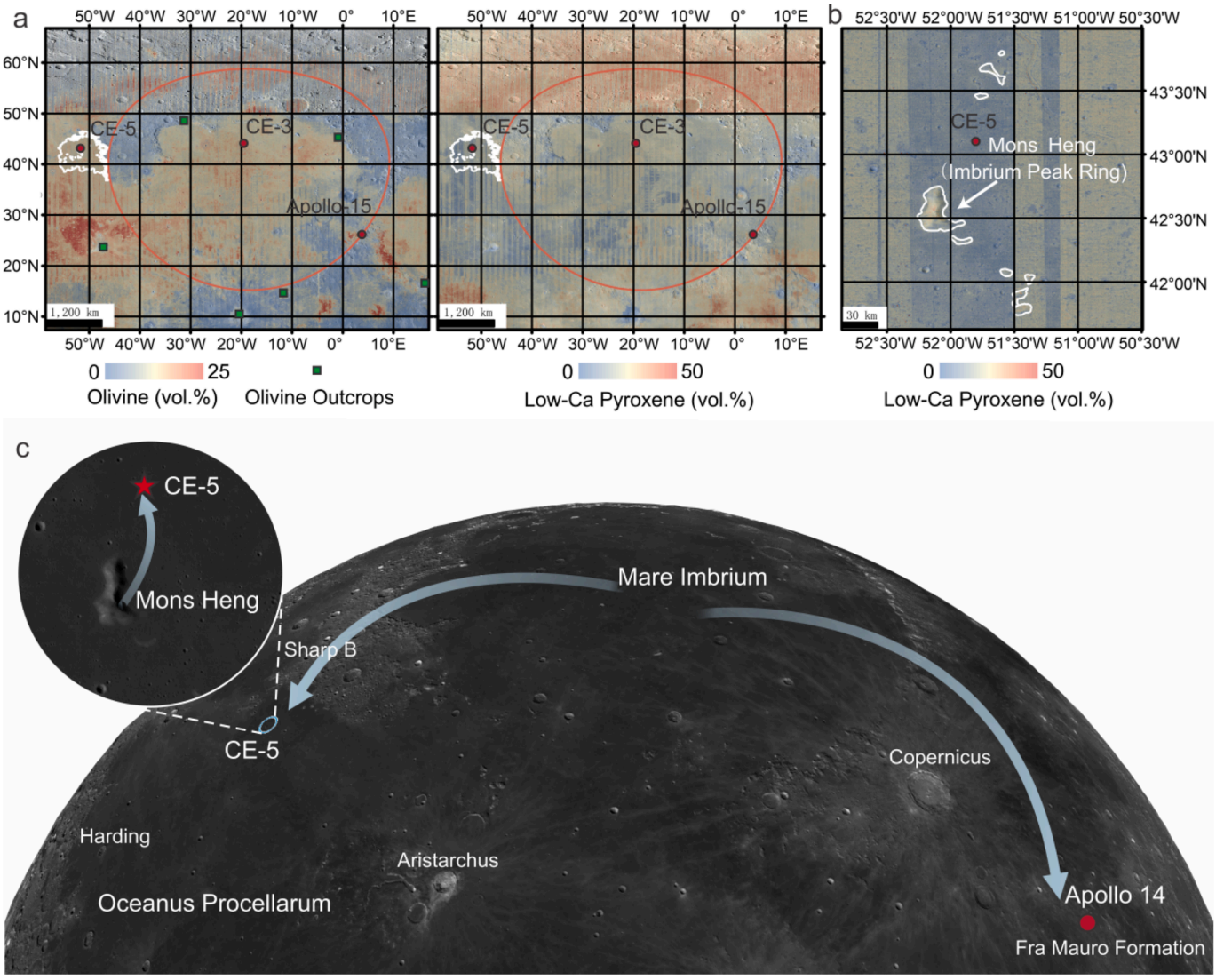

Fig. 4. Mineral abundance of the Imbrium basin region and inferred provenance of the exotic clast. (a) Olivine and LCP of the Imbrium basin region. The white line represents the Em4 mare unit CE-5 landing site. The red circle represents the Imbrium basin rim. Both datasets are based on Lemelin et al. (2016). (b) Focused view of the CE-5 landing site. Mons Heng (4th Imbrium Peak Ring) shows elevated LCP abundances (Qian et al., 2021a). c Speculation on source of the exotic clast: ejecta from the Imbrium basin reached the Apollo 14 landing site and Mons Heng; the exotic clasts were subsequently re-ejected by impacts to the Chang'e-5 landing site.

the LCP observed in impact-related settings—such as around the Imbrium and SPA basins—may have been produced by impact-induced recrystallization of olivine-rich lithologies. This is even more dramatic because in olivine and LCP mixtures, olivine will only have apparent spectral absorptions when its abundance reaches >20–30% (Sunshine et al., 1990). Consequently, the hypothesis that the lunar mantle is primarily composed of LCP warrants re-evaluation. Although we have proposed a convincing mechanism for the formation of LCP on the lunar surface through impact-induced processes, previous studies based on extensive remote-sensing observations, lunar sample analyses, and experimental petrological simulations have suggested the possibility that LCP may also occur in the lunar mantle (Yamamoto et al., 2023; Yamamoto et al., 2010; Moriarty et al., 2021). Therefore, LCP derived directly from excavation of the lunar mantle may also be present in lunar samples.

5. Conclusions

In this study, a unique exotic troctolitic clast exhibiting characteristic partial-melting textures was identified in the Chang'e-5 lunar soils. Detailed electron microscopy analyses provide compelling evidence that LCP formed through impact-induced partial melting of a troctolitic lithology, rather than representing a primary deep-seated lunar phase. Reverse zoning in olivine and the Ca- and Al-rich glassy matrix indicate that the LCP was produced by impact-induced partial melting of an olivine-rich troctolite. In addition, LCP grains embedded within the exotic clast exhibit elongated dendritic morphologies and chemical zoning consistent with crystallization from a rapidly cooled impact melt. Combined with remote-sensing observations and impact-ejecta simulations for the Chang'e-5 landing area, the results indicate that the precursor lithology of the studied exotic clast most likely originated from Imbrium ejecta.

Accordingly, the results demonstrate that LCP signatures observed around large lunar impact basins, such as Imbrium and SPA basins, may originate from impact-modified olivine-rich lithologies rather than from materials directly excavated from the deep lunar interior. Interpretation of excavated lithologies therefore requires caution, because some lithologies may be metamorphic or impact-modified in origin. Consequently, the longstanding debate over whether the lunar mantle is dominated by olivine or LCP may therefore warrant re-evaluation.

Data availability

Data are available through Figshare at https://doi.org/10.6084/m9.figshare.32188638.

CRediT authorship contribution statement

Yang Bai: Writing – review & editing, Writing – original draft, Methodology, Investigation, Formal analysis, Data curation, Conceptualization. **Zhuang Guo:** Writing – review & editing, Validation, Project administration, Methodology, Investigation, Funding acquisition, Conceptualization. **Yuqi Qian:** Writing – review & editing, Methodology, Investigation. **Shichuan Sun:** Writing – review & editing, Investigation. **Jingru Ma:** Investigation. **Kangjun Huang:** Writing – review & editing, Resources. **Li-Hui Chen:** Writing – review & editing, Resources. **Yunpeng Dong:** Writing – review & editing, Resources. **Simon A.T. Redfern:** Writing – review & editing, Investigation. **Charles K. Shearer:** Writing – review & editing, Methodology. **Guochun Zhao:** Supervision.

Declaration of competing interest

The authors declare that they have no known competing financial interests or personal relationships that could have appeared to influence the work reported in this paper.

Acknowledgements

We thank Satoru Yamamoto and the other reviewers for their constructive and insightful comments. The authors are grateful to the China National Space Administration (CNSA) for providing the Chang'e returned lunar samples. This work was supported by the National Natural Science Foundation of China (grant numbers 42678007 and 42303039).

Appendix A. Supplementary material

The supplementary material consists of two files that support the conclusions of this study and make all of the associated data publicly available, including: (I) Supplementary figures (PDF format) and (II) Supplementary tables (Excel format). Table S1 presents the mineral EPMA compositions (wt%) from the exotic clast, Table S2 provides the quantification results of atomic percent (%) of TEM-EDX analysis from pyroxenes, Table S3 provides major-element oxide data (wt%) from SEM-EDS line-scan analysis of olivine (Line 1) in the exotic troctolitic clast (corresponding to Fig. 1h) and Table S4 Supplementary Quantification results of Atomic percent (%) from SEM-EDS line-scan analysis of pyroxene (Line 2) in the exotic troctolitic clast (corresponding to Fig. 1h). Supplementary material to this article can be found online at https://doi.org/10.1016/j.gca.2026.09.038.

References

Aysal, N., Kurt, Y., Öztürk, H., Ildiz, G.O., Yesiltas, M., Laçin, D., Öngen, S., Nikitin, T., Fausto, R., 2023. Crystallization kinetics: relationship between crystal morphology and the cooling rate—applications for different geological materials. Crystals 13 (7), 1130.

Bouquain, S., Arndt, N., Faure, F., Libourel, G., 2014. An experimental study of pyroxene crystallization during rapid cooling in a thermal gradient: application to komatiites. Solid Earth 5 (2), 641–650.

Cao, H., Wang, C., Chen, J., Che, X., Fu, X., Shi, Y., Liu, D., Ling, Z., Qiao, L., Lu, X., 2022. A Raman spectroscopic and microimage analysis perspective of the Chang'e-5 lunar samples. Geophys. Res. Lett. 49 (13), e2022GL099282.

Che, X., Nemchin, A., Liu, D., Long, T., Wang, C., Norman, M.D., Joy, K.H., Tartese, R., Head, J., Jolliff, B., 2021. Age and composition of young basalts on the Moon, measured from samples returned by Chang'e-5. Science 374 (6569), 887–890.

Chen, Z., Zhao, Y., Chi, X., Yan, Y., Shen, J., Zou, M., Zhao, S., Liu, M., Yao, W., Zhang, B., 2023. Geological timescales' aging effects of lunar glasses. Sci. Adv. 9 (45), eadi6086.

Corrigan, G., 1982. Supercooling and the crystallization of plagioclase, olivine, and clinopyroxene from basaltic magmas. Mineral. Mag. 46 (338), 31–42.

Crites, S.T., Lucey, P.G., Taylor, G.J., 2015. The mafic component of the lunar crust: Constraints on the crustal abundance of mantle and intrusive rock, and the mineralogy of lunar anorthosites. Am. Mineral. 100 (8–9), 1708–1716.

Cushing, J.A., Taylor, G.J., Norman, M.D., Keil, K., 1999. The granulitic impactite suite: Impact melts and metamorphic breccias of the early lunar crust. Meteorit. Planet. Sci. 34 (2), 185–195.

Delano, J.W., 1986. Pristine lunar glasses: criteria, data, and implications. J. Geophys. Res. Solid Earth 91 (B4), 201–213.

Dence, M.R., Plant, A.G., 1972. Analysis of Fra Mauro samples and the origin of the Imbrium Basin, In: Proceedings of the Third Lunar Science Conference, Supplement 3, 379–399.

Dickey, J.O., Bender, P.L., Faller, J.E., Newhall, X.X., Ricklefs, R.L., Ries, J.G., Shelus, P. J., Veillet, C., Whipple, A.L., Wiant, J.R., Williams, J.G., Yoder, C.F., 1994. Lunar laser ranging: a continuing legacy of the Apollo Program. Science 265 (5171), 482–490.

Ding, C.-L., Nemchin, A., Johnson, T., Norman, M.D., Guan, Y., Tian, L.-L., Xie, W.-L., Li, L.-S., Zhou, S.-D., Xu, K.-X., 2025. A potential mantle origin for precursor rocks of high-Mg impact glass beads in Chang'e-5 soil. Sci. Adv. 11 (19), eadv9019.

Donaldson, C., Drever, H., Johnston, R., 1977. Supercooling on the lunar surface: a review of analogue information. Philos. Trans. R. Soc. Lond. Ser. A, Math. Phys. Sci. 285 (1327), 207–217.

Donaldson, C.H., 1979. An experimental investigation of the delay in nucleation of olivine in mafic magmas. Contrib. Miner. Petrol. 69 (1), 21–32.

Dowty, E., Keil, K., Prinz, M., 1974. Lunar pyroxene-phyric basalts: crystallization under supercooled conditions. J. Petrol. 15 (3), 419–453.

Faure, F., Trolliard, G., Nicollet, C., Montel, J.M., 2003. A developmental model of olivine morphology as a function of the cooling rate and the degree of undercooling. Contrib. Miner. Petrol. 145 (2), 251–263.

Fowler, G., Papike, J., Spilde, M., Shearer, C., 1994. Diogenites as asteroidal cumulates: Insights from orthopyroxene major and minor element chemistry. Geochim. Cosmochim. Acta 58 (18), 3921–3929.

Ginibre, C., Wörner, G., Kronz, A., 2007. Crystal zoning as an archive for magma evolution. Elements 3 (4), 261–266.

Gou, S., Di, K., Yue, Z., Liu, Z., He, Z., Xu, R., Lin, H., Liu, B., Peng, M., Wan, W., Wang, Y., Liu, J., 2019. Lunar deep materials observed by Chang'e-4 rover. Earth Planet. Sci. Lett. 528, 115829.

Gross, J., Hilton, A., Prissel, T.C., Setera, J.B., Korotev, R.L., Calzada-Diaz, A., 2020. Geochemistry and petrogenesis of Northwest Africa 10401: a new type of the Mg-suite rocks. J. Geophys. Res. Planets 125 (5), e2019JE006225.

Gross, J., Treiman, A.H., Mercer, C.N., 2014. Lunar feldspathic meteorites: constraints on the geology of the lunar highlands, and the origin of the lunar crust. Earth Planet. Sci. Lett. 388, 318–328.

He, Q., Cao, Z., Qian, Y., Hui, H., Baziotis, I., Xiao, L., Wang, Z., Luo, B., Li, Y., Ying, Z., 2024. Petrogenesis of magnesian troctolitic granulite clasts from Chang'e-5 drilling sample: Implications for the origin of ejecta material from lunar highlands. Icarus 408, 115853.

Heiken, G., Vaniman, D., French, B.M., 1991. Lunar sourcebook: a user's guide to the moon. Cambridge, UK.

Hess, P.C., 1994. Petrogenesis of lunar troctolites. J. Geophys. Res. Planets 99 (E9), 19083–19093.

Jolliff, B.L., Wieczorek, M.A., Shearer, C.K., Neal, C.R., 2006. New Views of the Moon. , Mineralogical Society of America, Chantilly, Virginia, p. 721.

Khan, A., Pommier, A., Neumann, G., Mosegaard, K., 2013. The lunar moho and the internal structure of the Moon: a geophysical perspective. Tectonophysics 609, 331–352.

Kirkpatrick, R.J., 1975. Crystal growth from the melt: a review. Am. Mineral. 60 (9–10), 798–814.

Kirkpatrick, R.J., 1983. Theory of nucleation in silicate melts. Am. Mineral. 68 (1–2), 66–77.

Klima, R.L., Pieters, C.M., Boardman, J.W., Green, R.O., Head III, J.W., Isaacson, P.J., Mustard, J.F., Nettles, J.W., Petro, N.E., Staid, M.I., 2011. New insights into lunar petrology: distribution and composition of prominent low-Ca pyroxene exposures as observed by the Moon Mineralogy Mapper (M3). J. Geophys. Res. Planets 116 (E6).

Lemelin, M., Lucey, P., Gaddis, L., Hare, T., Ohtake, M., 2016. Global map products from the Kaguya multiband imager at 512 ppd: minerals, FeO, and OMAT, 47th annual lunar and planetary science conference. p. 2994.

Li, C., Hu, H., Yang, M.-F., Pei, Z.-Y., Zhou, Q., Ren, X., Liu, B., Liu, D., Zeng, X., Zhang, G., 2022. Characteristics of the lunar samples returned by the Chang'E-5 mission. Natl. Sci. Rev. 9 (2), nwab188.

Li, Y., McCausland, P., Flemming, R., Osinski, G., 2025. Petrology and shock history of hybrid lunar feldspathic–troctolitic breccia Northwest Africa 11515. Meteorit. Planet. Sci. 60 (2), 347–370.

Lindstrom, M.M., Lindstrom, D.J., 1986. Lunar granulites and their precursor anorthositic norites of the early lunar crust. J. Geophys. Res. Solid Earth 91 (B4), 263–276.

Liu, T., Michael, G., Zhu, M.H., Wünnemann, K., 2021. Predicted sources of samples returned from Chang'e-5 landing region. Geophys. Res. Lett. 48 (8), e2021GL092434.

Long, T., Qian, Y., Norman, M.D., Miljkovic, K., Crow, C., Head, J.W., Che, X., Tartèse, R., Zellner, N., Yu, X., Xie, S., Whitehouse, M., Joy, K.H., Neal, C.R., Snape, J.F., Zhou, G., Liu, S., Yang, C., Yang, Z., Wang, C., Xiao, L., Liu, D., Nemchin, A., 2022. Constraining the formation and transport of lunar impact glasses using the ages and chemical compositions of Chang'e-5 glass beads. Sci. Adv. 8 (39), eabq2542.

Longhi, J., 1978. The distribution of Fe and Mg between olivine and lunar basaltic liquids. Geochim. Cosmochim. Acta 42, 1545–1558.

Lucey, P.G., Norman, J.A., Crites, S.T., Taylor, G.J., Hawke, B.R., Lemelin, M., Melosh, H. J., 2014. A large spectral survey of small lunar craters: implications for the composition of the lunar mantle. Am. Mineral. 99 (11–12), 2251–2257.
Marks, N., Borg, L., Shearer, C., Cassata, W., 2019. Geochronology of an Apollo 16 clast provides evidence for a basin-forming impact 4.3 billion years ago. J. Geophys. Res. Planets 124 (10), 2465–2481.
McCallum, I., O'Brien, H.E., 1996. Stratigraphy of the lunar highland crust; depths of burial of lunar samples from cooling-rate studies. Am. Mineral. 81 (9–10), 1166–1175.
Melosh, H., Kendall, J., Horgan, B., Johnson, B., Bowling, T., Lucey, P., Taylor, G., 2017. South Pole–Aitken basin ejecta reveal the Moon's upper mantle. Geology 45 (12), 1063–1066.
Miljković, K., Wieczorek, M.A., Collins, G.S., Solomon, S.C., Smith, D.E., Zuber, M.T., 2015. Excavation of the lunar mantle by basin-forming impact events on the Moon. Earth Planet. Sci. Lett. 409, 243–251.
Moriarty III, D.P., Dygert, N., Valencia, S.N., Watkins, R.N., Petro, N.E., 2021. The search for lunar mantle rocks exposed on the surface of the Moon. Nat. Commun. 12, 4659.
Morrison, R.H., Oberbeck, V.R., 1975. Geomorphology of crater and basin deposits - emplacement of the Fra Mauro Formation. In: Lunar Science Conference, 6th. Pergamon Press, Houston, Tex, pp. 2503–2530.
Morse, S., 1982. Adcumulus growth of anorthosite at the base of the lunar crust. J. Geophys. Res. Solid Earth 87 (S01), A10–A18.
Mullins, W.W., Sekerka, R., 1964. Stability of a planar interface during solidification of a dilute binary alloy. J. Appl. Phys. 35 (2), 444–451.
Nemchin, A., Pidgeon, R., Healy, D., Grange, M., Whitehouse, M., Vaughan, J., 2009. The comparative behavior of apatite-zircon U-Pb systems in Apollo 14 breccias: implications for the thermal history of the Fra Mauro Formation. Meteorit. Planet. Sci. 44 (11), 1717–1734.
Papike, J., 1996. Pyroxene as a recorder of cumulate formational processes in asteroids, Moon, Mars, Earth; reading the record with the ion microprobe. Am. Mineral. 81 (5–6), 525–544.
Papike, J., Fowler, G., Shearer, C., 1994. Orthopyroxene as a recorder of lunar crust evolution: an ion microprobe investigation of Mg-suite norites. Am. Mineral. 79 (7–8), 796–800.
Papike, J., Karner, J., Shearer, C., Burger, P., 2009. Silicate mineralogy of martian meteorites. Geochim. Cosmochim. Acta 73 (24), 7443–7485.
Potter, R.W., Collins, G.S., Kiefer, W.S., McGovern, P.J., Kring, D.A., 2012. Constraining the size of the South Pole-Aitken basin impact. Icarus 220 (2), 730–743.
Qian, Y., Xiao, L., Head, J.W., van der Bogert, C.H., Hiesinger, H., Wilson, L., 2021a. Young lunar mare basalts in the Chang'e-5 sample return region, northern Oceanus Procellarum. Earth Planet. Sci. Lett. 555, 116702.
Qian, Y., Xiao, L., Head, J.W., Wöhler, C., Bugiolacchi, R., Wilhelm, T., Althoff, S., Ye, B., He, Q., Yuan, Y., 2021b. Copernican-aged (<200 Ma) impact ejecta at the Chang'e-5 landing site: statistical evidence from crater morphology, morphometry, and degradation models. Geophys. Res. Lett. 48 (20), e2021GL095341.
Roberts, S., McCanta, M., Jean, M., Taylor, L., 2019. New lunar meteorite NWA 10986: a mingled impact melt breccia from the highlands—A complete cross section of the lunar crust. Meteorit. Planet. Sci. 54 (12), 3018–3035.
Sethian, J.A., Straint, J., 1992. Crystal growth and dendritic solidification. J. Comput. Phys. 98 (2), 231–253.
Shearer, C.K., Elardo, S.M., Petro, N.E., Borg, L.E., McCubbin, F.M., 2015. Origin of the lunar highlands Mg-suite: an integrated petrology, geochemistry, chronology, and remote sensing perspective. Am. Mineral. 100 (1), 294–325.
Shearer, C.K., Papike, J.J., 2005. Early crustal building processes on the Moon: models for the petrogenesis of the magnesian suite. Geochim. Cosmochim. Acta 69 (13), 3445–3461.
Shearer, C.K., Papike, J.J., 1993. Basaltic magmatism on the Moon: a perspective from volcanic picritic glass beads. Geochim. Cosmochim. Acta 57 (19), 4785–4812.
Sheng, S.-Z., Wang, S.-J., Li, Q.-L., Wu, S., Wang, H., Hua, J.-X., Chen, Z., Hao, J.-H., Zhang, B., He, Y., 2025. Lunar primitive mantle olivine returned by Chang'e-6. Nat. Commun. 16 (1), 3759.
Shervais, J.W., McGee, J.J., 1999a. KREEP cumulates in the western lunar highlands: ion and electron microprobe study of alkali-suite anorthosites and norites from Apollo 12 and 14. Am. Mineral. 84 (5–6), 806–820.
Shervais, J.W., McGee, J.J., 1999b. Petrology of the Western Highland Province: ancient crust formation at the Apollo 14 site. J. Geophys. Res. Planets 104 (E3), 5891–5920.
Shervais, J.W., Taylor, L.A., Laul, J., 1983. Ancient crustal components in the Fra Mauro breccias. J. Geophys. Res. Solid Earth 88 (S01), B177–B192.
Snyder, G.A., Neal, C.R., Taylor, L.A., Halliday, A.N., 1995. Processes involved in the formation of magnesian-suite plutonic rocks from the highlands of the Earth's Moon. J. Geophys. Res. Planets 100 (E5), 9365–9388.
Stöffler, D., Hamann, C., Metzler, K., 2018. Shock metamorphism of planetary silicate rocks and sediments: proposal for an updated classification system. Meteorit. Planet. Sci. 53 (1), 5–49.
Streck, M.J., 2008. Mineral textures and zoning as evidence for open system processes. Rev. Mineral. Geochem. 69 (1), 595–622.
Sun, L., Lucey, P.G., 2024. Lunar mantle composition and timing of overturn indicated by Mg# and mineralogy distributions across the South Pole-Aitken basin. Earth Planet. Sci. Lett. 643, 118931.
Sunshine, J.M., Pieters, C.M., Pratt, S.F., 1990. Deconvolution of mineral absorption bands: an improved approach. J. Geophys. Res. Solid Earth 95 (B5), 6955–6966.
Tian, H.-C., Wang, H., Chen, Y., Yang, W., Zhou, Q., Zhang, C., Lin, H.-L., Huang, C., Wu, S.-T., Jia, L.-H., 2021. Non-KREEP origin for Chang'e-5 basalts in the Procellarum KREEP Terrane. Nature 600 (7887), 59–63.
Wang, Z., Tian, W., Wang, W.-R., Prissel, T.C., Di, Y., Qian, Y., Liu, P.-P., Fa, W., Su, A., 2025. Genesis and timing of KREEP-free lunar Mg-suite magmatism indicated by the first norite meteorite Arguin 002. Commun. Earth Environ. 6 (1), 170.
Wang, Z., Zong, K., Li, Y., Li, J., He, Q., Zou, Z., Becker, H., Moynier, F., Day, J.M., Zhang, W., 2024. Young KREEP-like mare volcanism from Oceanus Procellarum. Geochim. Cosmochim. Acta 373, 17–34.
Warren, P.H., 1993. A concise compilation of petrologic information on possibly pristine nonmare Moon rocks. Am. Mineral. 78 (3–4), 360–376.
Wieczorek, M.A., Jolliff, B.L., Khan, A., Pritchard, M.E., Weiss, B.P., Williams, J.G., Hood, L.L., Righter, K., Neal, C.R., Shearer, C.K., 2006. The constitution and structure of the lunar interior. Rev. Mineral. Geochem. 60 (1), 221–364.
Wieczorek, M.A., Neumann, G.A., Nimmo, F., Kiefer, W.S., Taylor, G.J., Melosh, H.J., Phillips, R.J., Solomon, S.C., Andrews-Hanna, J.C., Asmar, S.W., 2013. The crust of the Moon as seen by GRAIL. Science 339 (6120), 671–675.
Yakovlev, O., Gerasimov, M., Dikov, Y.P., 2011. Estimation of temperature conditions for the formation of HASP and GASP glasses from the lunar regolith. Geochem. Int. 49 (3), 213–223.
Yamamoto, S., Nagaoka, H., Ohtake, M., Kayama, M., Karouji, Y., Ishihara, Y., Haruyama, J., 2023. Lunar mantle composition based on spectral and geologic analysis of low-Ca pyroxene-and olivine-rich rocks exposed on the lunar surface. J. Geophys. Res. Planets 128 (5), e2023JE007817.
Yamamoto, S., Nakamura, R., Matsunaga, T., Ogawa, Y., Ishihara, Y., Morota, T., Hirata, N., Ohtake, M., Hiroi, T., Yokota, Y., 2010. Possible mantle origin of olivine around lunar impact basins detected by SELENE. Nat. Geosci. 3 (8), 533–536.
Yamamoto, S., Ohtake, M., Karouji, Y., Kayama, M., Nagaoka, H., Ishihara, Y., Haruyama, J., 2022. Global distribution and geological context of co-existing occurrences of Olivine-Rich and plagioclase-rich materials on the lunar surface. J. Geophys. Res. Planets 127 (2), e2021JE007077.
Yang, W., Chen, Y., Wang, H., Tian, H.-C., Hui, H., Xiao, Z., Wu, S.-T., Zhang, D., Zhou, Q., Ma, H.-X., Zhang, C., Hu, S., Li, Q.-L., Lin, Y., Li, X.-H., Wu, F.-Y., 2022. Geochemistry of impact glasses in the Chang'e-5 regolith: constraints on impact melting and the petrogenesis of local basalt. Geochim. Cosmochim. Acta 335, 183–196.
Zeng, X., Li, X., Liu, J., 2023. Exotic clasts in Chang'e-5 regolith indicative of unexplored terrane on the Moon. Nat. Astron 7 (2), 152–159.
Zong, K., Wang, Z., Li, J., He, Q., Li, Y., Becker, H., Zhang, W., Hu, Z., He, T., Cao, K., 2022. Bulk compositions of the Chang'E-5 lunar soil: insights into chemical homogeneity, exotic addition, and origin of landing site basalts. Geochim. Cosmochim. Acta 335, 284–296.